SECOND EDITION

High-Resolution Mapping of Two-Dimensional Lattice Distortions in Ion-Implanted Crystals from X-Ray Diffractometry Data

A. Yu. NIKULIN and T. E. GUREYEV*1

School of Physics, University of Melbourne, Parkville, Victoria 3052, Australia

A. W. STEVENSON and S. W. WILKINS

CSIRO Division of Materials Science & Technology, Private Bag 33, Rosebank MDC, Clayton, Victoria 3169, Australia

H. HASHIZUME*2

Research Laboratory of Engineering Materials, Tokyo Institute of Technology, Nagatsuta, Midori, Yokohama 226, Japan

and D. COOKSON

Australian National Beamline Facility, Photon Factory, National Laboratory for High Energy Physics, Oho, Tsukuba 305, Japan

(Received: ; accepted)

Synopsis for inclusion in the Table of Contents:

Two-dimensional lattice distortions in near-surface layers of silicon (111) crystals implanted with B^+ ions of 100 keV energy through a periodic oxide mask pattern have been mapped out with spatial resolutions of 0.016 and 0.265 μm in the depth and lateral directions respectively using triple-crystal synchrotron X-ray diffractometry data.

keywords:

lattice strain map, model-independent reconstruction, synchrotron X-ray diffractometry, phase retrieval, rocking curve, ion implantation, superlattice modulation, submicron spatial resolution

Manuscript submitting author: H. Hashizume

Fax: +81-45-922-5169

email: hhashizu@nc.titech.ac.jp

---

*1 Also at CSIRO Division of Materials Science & Technology, Clayton.

*2 To whom all correspondence should be addressed.

Abstract

The triple-crystal synchrotron X-ray diffractometry data described in Nikulin, Stevenson, Hashizume, Wilkins, Foran, Cookson & Garrett (*J. Appl. Cryst.* 28, 57-60 (1995)) has been analyzed to map out two-dimensional (2D) lattice distortions in silicon (111) crystals implanted with B^+ ions of 100 keV energy through a periodic SiO_2 strip pattern. The lateral periodic structure produced a series of satellite reflections associated with the 111 Bragg peak. The 2D reconstruction incorporates the use of the Petrashen-Chukhovskii method, which retrieves the phases of the Bragg waves for these satellite reflections, together with that for the fundamental. The finite Fourier series is then synthesized with the relative phases determined. Localized distortions perpendicular to the surface arising from deposited B^+ ions in near-surface layers of the crystal are clearly displayed with spatial resolutions of 0.016 and 0.265 μm in the depth and lateral directions respectively. For a sample with the oxide layer removed from the surface, two equally plausible strain maps have been obtained by assigning relative phases to eleven satellites using a sequential trial method and a minimum-energy method. Failed map reconstructions for the oxide-covered sample are discussed in terms of the non-unique solutions of the Petrashen-Chukhovskii phase-recovery algorithm and the ambiguous phases determined for the satellites.

1. Introduction

In a recent paper we have demonstrated that lattice distortions in surface layers of ion-implanted silicon crystals can be mapped out with submicron spatial resolution using high-resolution X-ray diffractometry data collected at a synchrotron source (Nikulin, Sakata, Hashizume & Petrashen, 1994). The maps show the two-dimensional profile of the lattice distortion perpendicular to the surface as a function of lateral position and depth in crystals

implanted with 300 keV B^+ ions through a periodic surface oxide strip pattern. The displayed maps resolve localized strain in silicon at 0.35 and 1.05 μm depths due to the ions penetrating through the SiO_2 mask film and open regions. The analysis of the X-ray data used an algorithm which retrieved the phase information for the Bragg-diffracted waves, thus enabling *ab-initio* determination of the strain profiles in single crystals. The algorithm was originally developed by Petrashen & Chukhovskii (1989) and extended by Goureev, Nikulin & Petrashen (1992) to two-dimensional distortions involving periodic superlattice modulations in the lateral direction.

The spatial resolution achieved by Nikulin, Sakata, Hashizume *et al.* (1994) was 0.05 and 0.32 μm in the depth and lateral directions respectively. These were defined by the momentum transfer range of $q_x = -1.4 \sim +1.4 \times 10^{-3}$ nm^{-1} (in-plane direction) and $q_z = -2 \sim +2 \times 10^{-3}$ nm^{-1} (surface normal direction) around the Si 111 Bragg point, measured with the triple-crystal diffractometer on beamline 14B at the Photon Factory synchrotron source. We have demonstrated that a much larger reciprocal-space area can be explored on the diffractometer installed on beamline 20B when used with a four-reflection diffracted-beam analyzer (Nikulin, Stevenson, Hashizume *et al.*, 1995). The present paper reports the analysis of the latter data and presents strain maps believed to have the highest spatial resolutions thus far. We start by outlining in Sec. 2 the experiment and data collection, followed by a description in Sec. 3 of the 2D strain map reconstruction procedure where we propose a local minimum-energy criterion for the determination of satellite phases. High-resolution maps are presented in Sec. 4. Section 5 contains a discussion of the maps obtained and the associated ambiguity problems.

2. Experimental

The experiments were performed at the Australian National Beamline Facility

(ANBF), located on BL-20B of the Photon Factory in Japan, using a high-resolution multipurpose X-ray diffractometer "BIGDIFF" (Barnea *et al.*, 1989; 1992). The sample studied is part of a symmetric Si (111) wafer which was implanted with 100 keV energy B^+ ions (dose 5×10^{15} cm^{-2}) through an SiO_2 strip mask pattern (0.5 μm thick) with a 5.83 μm period and 4 μm open regions. The oxide strips had edges parallel to the $[1\bar{1}0]$ direction. Such a mask was used to create a one-dimensional superstructure modulation in the sample crystal. In the set-up shown in Fig. 1, the primary monochromator used a two-reflection symmetric Si (111) monolithic crystal with water-cooling of the first face, to extract 1.54 Å X-rays from a bending-magnet source. A slit and anti-scatter shielding produced a beam of 0.1 mm in vertical height (in the plane of diffraction) and 2.0 mm in horizontal width, which was incident on the sample having azimuthal orientation such that the plane of diffraction was perpendicular to the oxide strips. The analyzer crystal, mounted on the detector arm together with a scintillation counter, was a four-reflection symmetric Si (111) monolithic crystal. The overall arrangement of these elements was (+, −, +, −, +, −, +). An automatic attenuator inserter was employed after the monochromator to cope with the intensity range of 7 decades.

The experiments involved measurement of triple-crystal intensity maps in the vicinity of the Si 111 Bragg peak by performing, in air, a series of sample (ω) scans for fixed positions of the analyzer/detector (2θ). The nominal step sizes were 0.0003° in ω and 0.0044° in 2θ. The parallelogram covered in (ω, 2θ) space (where ω and 2θ are plotted as orthogonal axes) has sides parallel to the ω axis and to the line given by $2\theta = 2\omega$. The point $\omega = 2\theta = 0$ is located at the Bragg peak (fundamental reflection) position. The line $2\theta = 2\omega$ coincides with the direction of crystal-truncation-rod (CTR) scattering from a symmetric sample. The periodic superstructure in our samples resulted in a series of satellite reflections, each having its

own CTR scattering. The intensity distribution along the CTR for the nth satellite is denoted by I_n in the following discussion ($n = 0$ for the fundamental reflection).

Intensity distributions in angular (ω, 2θ) space are transformed to reciprocal (q_x, q_z) space using

$$q_x = (2\omega - 2\theta)\sin\theta_B / \lambda, \qquad (1)$$

$$q_z = 2\theta\cos\theta_B / \lambda, \qquad (2)$$

where θ_B is the Bragg angle and λ the X-ray wavelength. The scanned areas are rectangular in reciprocal space, with the CTR direction parallel to the q_z axis for a symmetric sample. The nominal step sizes correspond to 1.7×10^{-5} in q_x and 4.8×10^{-4} nm^{-1} in q_z. The corresponding scan ranges are $\pm 2.35\times 10^{-3}$ and $\pm 3.1\times 10^{-2}$ nm^{-1}. The Darwin width of our sample is equivalent to 4.7×10^{-4} nm^{-1} in q_z. Fig. 2 shows the 2D intensity distribution in reciprocal space for the sample with the oxide mask removed in HF solution. A similar plot for the sample with the oxide layer present on the surface was shown in the previous paper (Nikulin, Stevenson, Hashizume *et al.*, 1995). The sample had the (111) Bragg planes slightly inclined to the surface. The q_z component of the scattering vector was thus slightly off the CTR direction, with the q_x component slightly directed into the crystal. The intensity distribution in Fig. 2 is nearly symmetric in the q_x direction and asymmetric in the q_z direction. The latter feature indicates near-surface layers strained in the depth direction.

Fig. 3 shows, on a logarithmic scale, ω-slice scans through the Bragg peaks for the samples with and without the oxide layer. 12 or 13 satellites are clearly resolved on either side of the central peaks. The satellite peaks are more enhanced in the oxide-covered sample (Fig. 3a) than in the oxide-removed sample (b), in agreement with the larger strain gradients

expected at the edges of the SiO_2 strips in the former sample. Our experiment used a highly parallel primary X-ray beam with an angular divergence of $\sim 30\ \mu$rad in the plane of diffraction. The obtained data are not free, however, from contamination, albeit small, by thermal diffuse scattering (TDS), Compton scattering, and the dynamical tails of the monochromator and analyzer crystals. We thus use only the peak intensity information of each satellite, and disregard other data points.

The intensity distributions along the crystal truncation rods associated with the fundamental ($n = 0$) and satellite ($n = 1, 2, ..., 11$) reflections are shown in Fig. 4 for the two samples. The intensity profiles of the fundamental look like a conventional double-crystal rocking curve from an ion-implanted crystal. Monoenergetic ions implanted along the Si [111] axis channeled through the surface layer and produced a damaged layer at a well-defined depth determined by the projected penetration of the ions. This results in a bi-crystal structure with a less distorted thin surface layer on top of the damaged layer. A rocking curve from such a structure shows symmetrical intensity oscillations on both sides of the central peak with a subpeak separation given by $\lambda/2t\cos(\theta_B)$, where t is the thickness of the surface layer. In the case where the surface layer is nonuniformly strained in depth, the rocking-curve profile tends to be asymmetrical. A comparison with the previous CTR profiles (Nikulin, Sakata, Hashizume *et al.*, 1994) indicates that subpeaks are much better resolved in the present samples. The calculated penetration of 100 keV B^+ ions channeling along the silicon [111] axis is 0.5 μm (Hobler, 1995), as compared to 1.1 μm for 300 keV B^+ ions.

The fact that the scattering vector for the fundamental reflection is nearly parallel to the surface normal of the sample (or the z axis) means that the X-ray data only involve information on the z component of the atomic displacements. Information on the x component could be obtained by experiments using a scattering vector with a non-zero q_x component.

For further experimental details, see Nikulin, Stevenson, Hashizume *et al.* (1995).

3. Strain map reconstruction procedure

The method of *ab-initio* strain map reconstruction was described in the previous publications (Goureev, Nikulin & Petrashen, 1992; Nikulin, Sakata, Hashizume *et al.*, 1994). Here we outline it and make some new comments.

Let us consider a crystal in the form of a thick plate with lattice distortions uniform in a direction (y) parallel to the surface, but varying along the perpendicular direction (x) in the surface plane and in the crystal depth (z). Such distortions can be described via a 2D vector field of atomic displacements:

$$\mathbf{u}(\mathbf{r}) = \mathbf{u}(x, z) = \{u_x(x, z),\ u_z(x, z)\}. \qquad (3)$$

We assume the distortions to be weak, so that

$$\left| \frac{\partial u_i}{\partial r_j} \right| << 1 \quad (i = 1, 2;\ j = 1, 2;\ u_1 = u_x,\ u_2 = u_z,\ r_1 = x,\ r_2 = z). \qquad (4)$$

Then the Fourier coefficients of the susceptibility of the distorted crystal can be expressed as a perturbation of the susceptibility of a perfect crystal (Takagi, 1969):

$$\chi_h(x, z) = \chi_h^{ideal} \exp\{2\pi i \mathbf{h} \cdot \mathbf{u}(x, z)\}, \qquad (5)$$

where χ_h^{ideal} is the Fourier coefficient of the dielectric susceptibility of an ideal crystal associated with the reciprocal lattice vector h. If the displacements are periodic in x with period a, $\chi_h(x, z)$ can be expanded into a Fourier series:

$$\chi_h(x, z) = \sum_n \chi_h^n(z) \exp(2\pi i n x/a). \qquad (6)$$

In the kinematical approximation the absolute values of the Fourier transforms $\widetilde{\chi}^{n}_{h}(q_z)$ of the Fourier components $\chi^{n}_{h}(z)$ are proportional to the square roots of the CTR intensity distributions $I_n(q_z)$:

$$|\,\widetilde{\chi}^{n}_{h}(q_z)\,| \sim [I_n(q_z)]^{1/2}. \qquad (7)$$

Hence, the absolute values of the complex functions $\widetilde{\chi}^{n}_{h}(q_z)$ can be obtained directly from experimental data. Formula (7) is not as trivial as it may seem (Goureev, Nikulin & Petrashen, 1992). We apply the Petrashen-Chukhovskii method for each $n = 0, \pm 1, \pm 2, \ldots, \pm N$ (N is the number of measured satellites, $n = 0$ corresponds to the fundamental harmonic) to retrieve the phases $\phi_n(q_z) = \arg\{\widetilde{\chi}^{n}_{h}(q_z)\}$ of the functions $\widetilde{\chi}^{n}_{h}(q_z)$ from their absolute values. We do not discuss here this 1D phase recovery procedure (for details see Petrashen & Chukhovskii (1989) and Goureev, Nikulin & Petrashen (1992)). For the purpose of 2D map reconstruction it is important to note that the 1D phase $\phi_n(q_z)$ can be always found only up to an arbitrary additive constant γ_n. Such a constant is insignificant for 1D problems, as $\phi_n(q_z)$ and $\phi_n(q_z) + \gamma_n$ with $\gamma_n = constant$ are equivalent. These "relative phases" γ_n become important, however, in 2D cases where the Fourier synthesis (6) is performed in order to obtain the function $\chi_h(x, z)$. Assume that the phases $\phi_n(q_z)$ have been recovered and the Fourier components $\chi^{n}_{h}(z)$ of the crystal susceptibility have been obtained from the complex functions

$$\widetilde{\chi}^{n}_{h}(q_z) = [I_n(q_z)]^{1/2}\exp\{i\phi_n(q_z)\} \qquad (8)$$

by the inverse Fourier transform. Then the finite Fourier sums

$$\chi^{(N)}_{h}(x, z) = \sum_{n=-N}^{N} \chi^{n}_{h}(z)\,\exp(i\gamma_n)\,\exp(2\pi inx/a) \qquad (9)$$

will give different 2D functions $\chi^{(N)}_{h}(x, z)$ for different sets of relative phases $\{\gamma_0, \gamma_1, \ldots, \gamma_N\}$. As a result, we will have a continuum of different distri-

butions of susceptibility and the corresponding continuum of different displacement fields

$$u_H(x, z) = (2\pi h)^{-1} \arg\{\chi_H^{(N)} / \chi_H^{ideal}\}, \qquad (10)$$

where $u_H(x, z)$ is the projection of the vector field $\mathbf{u}(x, z)$ onto the reciprocal lattice vector $\mathbf{h}$ (see (5)). Goureev, Nikulin & Petrashen (1992) proposed a method which, in the case of symmetric distortions with $u_H(a - x, z) = u_H(x, z)$, allows one to reduce the ambiguity of the choice of $N + 1$ arbitrary real constants (relative phases) to the choice of N signs $\{\sigma_1, \sigma_2, ..., \sigma_N\}$, each $\sigma_k = \pm 1$. This reduction exploits the presence of the perfect crystal substrate under the thin surface layer. The result is consistent with the mirror symmetry of the 1D structures responsible for the satellites in our samples. After such a reduction formula (9) can be rewritten as

$$\chi_H^{(N)}(x, z) = \sum_{n=-N}^{N} \chi_H^n(z) \exp(i\pi \sigma_n/2) \exp(2\pi inx/a), \qquad (11)$$

where $\sigma_0 = 0$, $\sigma_n = \pm 1$ for $n = 1, 2, ..., N$, $\sigma_{-n} = \sigma_n$. Thus, we have 2^N different 2D profiles of susceptibility corresponding to different choices of the signs $\{\sigma_1, \sigma_2, ..., \sigma_N\}$, and 2^N corresponding profiles $u_H(x, z)$, obtained from the given set of 1D Fourier harmonics $\chi_H^n(z)$, $n = \pm 1, \pm 2, ..., \pm N$.

In principle, the relative phases γ_n or signs σ_n could be recovered if interference patterns between CTRs are measured. In our experiment, however, the angular distance between satellites on the ω-scan rocking curves is greater than the width of individual peaks, hence each satellite is virtually independent of the others. The peak intensities are the only data that can be used for structure analysis of the sample. For the reasons explained in the previous section, the intensity values measured in between the peaks cannot easily be related to the sample parameters. On the other hand, the knowledge of peak intensities is insufficient for the determination of the

relative phases (Millane, 1990). We have therefore to use some *a priori* information about the sample in order to find a plausible distribution of the crystal distortions among the possible solutions (10)-(11).

Previously we used a model function for an x-section of the displacement profile $u_h(x, z)$ at some fixed depth $z = z_0$, $f_{model}(x) = u_h(x, z_0)$, to determine the signs σ_n (Goureev, Nikulin & Petrashen, 1992; Nikulin, Sakata, Hashizume *et al.*, 1994). This method works for simple profiles with an easily predictable shape of such an x-section. The model function can be constructed, for example, on the basis of a theoretical model of the crystal deformations or Monte-Carlo simulations of ion implantation (Goureev, Nikulin & Petrashen, 1992). Note that it is not necessary to define the exact shape of such a section $f_{model}(x) = u_h(x, z_0)$ in order to determine $u_h(x, z)$ unambiguously. The only information needed is the signs of the Fourier coefficients of $f_{model}(x)$, and these signs are stable with respect to small variations of the model function and the depth z_0. If $g(x)$ is a function with small magnitude, then the sign of the nth Fourier coefficient of the function $f_{model}(x) + g(x)$ will be the same as that of $f_{model}(x)$, unless the nth Fourier coefficient of $f_{model}(x)$ is itself small. When the nth Fourier coefficient is small, the change of its sign usually has only weak influence on the result. This stability is generally higher for the lower-order Fourier coefficients.

Another method of the determination of the signs σ_n is the successive trial of different signs, starting from $n = 1$ and gradually treating $n = 2, 3, \ldots$. The choice of the signs can be made at each step if the sought map is known approximately. The main factors governing the sign choice are the depth of the damaged layer and the masked/open area ratio. The average penetration of ions and their concentration profile can be evaluated from Monte-Carlo simulations for a given ion species, implantation energy and orientation, and dose. The masked/open area ratio can be measured under an optical microscope. Other pieces of information also help the sign deter-

mination. Again, for the relatively smooth profiles with weak higher harmonics this method works well. It fails, however, for complicated distortions with strong high Fourier components, like in our sample with the patterned SiO_2 layer present on the surface.

In this work we also consider a method for the selection of satellite signs based on the local minimum-energy principle. Assuming all the deformations in the crystal to be elastic, we can write for the strain energy of a deformed crystal

$$W[\mathbf{du}] = \iiint w(x, y, z)\, dxdydz, \tag{12}$$

where the integration is over the crystal volume,

$$w(x, y, z) = (1/2) \sum\sum c_{ij}\, \varepsilon_i \varepsilon_j \tag{13}$$

is the density of the strain energy, c_{ij} are the elastic stiffness constants of the crystal and ε_i are the components of the strain tensor (Nye, 1985). For the 2D deformations of a silicon crystal we obtain

$$w = c_{11}[(\partial_z u_z)^2 + \partial_x u_x)^2] + 2c_{12}(\partial_x u_x)(\partial_z u_z) + c_{44}[\partial_x u_x + \partial_z u_z]^2, \tag{14}$$

with $c_{11} = 16.6$, $c_{12} = 6.4$, $c_{44} = 7.96$ ($\times 10^{11}$ dyn/cm^2). As any elastic strains in a solid body in thermal equilibrium must distribute so that the corresponding strain energy is minimal, we can look for the field of atomic displacements $\mathbf{u}(x, z)$ that gives the minimum value to the functional (12) among all possible solutions. We admit that such an approach has a number of apparent limitations. Crystals implanted with high-energy ions at room temperature include complex lattice defects, of which concentrations and distributions are far from thermal equilibrium. For such samples, the real profile $\mathbf{u}(x, z)$ may not provide the overall (global) minimum to the functional (12). However, as at room temperature the relaxation of elastic strains

occurs on a much shorter time scale than the diffusion of defects and other atomic processes changing the entropy, it is conceivable that the real distribution $u(x, z)$ provides a local minimum for $W[du]$ among the sufficiently close profiles. One would need the data of two different reflections with non-parallel projections of the vectors h_1 and h_2 on the (x, z)-plane in order to obtain both components of the 2D vector field $\mathbf{u}(x, z) = \{u_x(x, z), u_z(x, z)\}$ and calculate all the corresponding components of the strain tensor ∂_{xx}, ∂_{zx}, ∂_{xz} and ∂_{zz}. If such data are available, it is possible to use formulae (8)–(9) to construct the 2^N different displacements fields $\mathbf{u}(x, z)$ corresponding to the different combination of signs σ_n, find the corresponding values of the energy functional $W[du]$ using (12)–(14) and select those combinations of signs that provide local minima for $W[du]$. This approach can be effective in conjunction with the above methods of successive selection and model function. The latter may be used for the initial selection of the signs of the lower-order Fourier harmonics. Then the (local) minimum-energy criterion can be applied for the selection of the signs of higher-order Fourier harmonics.

Our experiments only provide the information about the z component $u_z(x, z)$ of displacements, allowing us to evaluate only the ∂_{xz} and ∂_{zz} components of the tensor. To evaluate the ∂_{xx} and ∂_{zx} components we need another experiment using a set of net planes inclined to the surface about the y axis. We will put here $\partial_{xx} = \partial_{zx} = 0$ for a first approximation.

4. High-resolution strain maps for ion-implanted crystals

Fig. 5 shows the two-dimensional maps of the z-derivative of the projection of the displacement field (u_x, u_z) onto the reciprocal lattice vector, $(1/h)d(hu_z)/dz$, in a thin surface layer of the oxide-removed sample. The vertical axis represents the relative change of the interplanar spacing,

$\Delta d/d$, in a direction nearly perpendicular to the surface. The map in Fig. 5(a) was constructed by Fourier synthesizing twelve 1D solutions obtained with the Petrashen-Chukhovskii method for the fundamental and 11 satellite reflections ($n = 0$ to ± 11). The signs of the latter reflections were determined with the sequential trial method. We also tried the model-function method of the relative-phase determination, using similar $f_{model}(x)$ to the ones used in Nikulin, Sakata, Hashizume *et al.* (1994). The same signs were found for the low-order satellites, but different signs for some higher harmonics, which led to unreasonable maps with peculiar thin peaks at 0.34 μm depth. In Fig. 5(a) are seen large strain peaks at 0.34 μm depth, which are due to the 100 keV B^+ ions incident on the mask gap regions. These peaks are much better resolved, in both lateral and depth directions, than in the similar map shown in Fig. 4(c) of Nikulin, Sakata, Hashizume *et al.* (1994). The latter reconstruction used 5 satellites ($n = \pm 5$) observed from a similar Si(111) sample but implanted with 300 keV B^+ ions to the same dose. The lateral resolution in the present map is 0.265 μm, which is sufficiently high to resolve the large valleys between the main peaks, as well as the shallow dips on the summits of the peaks. The large valleys, representing the shadows of the strip masks present on the sample surface at the time of ion implantation, were only poorly resolved in the previous map. The main peaks have a height of 2×10^{-3}, which is three times higher than in the previous map. This is consistent with the larger induced lattice strain expected for the 100 keV implantation, as well as the depth resolution of 160 Å achieved here as compared with 500 Å in the previous study. The half width of the main peak in Fig. 5(a) is $\sim$0.1 μm in the depth direction, implying the thickness of the damaged layer. We will attempt in a later section to relate the observed strain peaks to the types and distributions of lattice defects in ion-implanted silicon crystals. The projected penetration of 100 keV B^+ ions in SiO_2 is 0.38 μm (Hobler, 1995), which is smaller than the 0.5 μm

thickness of the actual mask layer. This explains the absence of peaks in the masked regions in Fig. 5(a). The short-period lateral oscillations prevailing in the entire map are artifacts, produced by the limited data resolution in this direction (see below). This type of oscillation was suppressed in the previous maps by applying a smoothing scheme.

A separate reconstruction using the same satellite solutions but with the signs determined according to the minimum-energy criterion produced a slightly different map (Fig. 5b). The minimum-energy phase set was different from the one obtained by the sequential trial method in the $n = 3$ and 6 satellites. The reversed signs of these reflections may be related to the 1 : 3 ratio of the oxide-strip width to the pattern period in our sample, which can affect every third harmonic. An effect of the differently phased satellites is evident in the central humps seen in the summits of the main strain peaks at 0.34 μm depth in Fig. 5(b). Fig. 6 shows the top view of the map in Fig. 5(a), which plots $\Delta d/d$ on a linear gray scale. The plot reveals low strain ridges extending from the edges of the surface SiO_2 strips which were used at the time of boron implantation and then removed. The concentrated strain field at the film edges may have disturbed the Si [111] channels for the B^+ ions. One can count 11 weak fringes over a unit period in the lateral direction, which are artifacts produced by the truncated Fourier synthesis. We have no evidence to favor one map over the other: the two maps in Fig. 5(a) and (b) are equally plausible.

In contrast to the reasonable maps for the oxide-removed sample, no acceptable map was gained for the oxide-covered sample with any of the phase determination methods. Fig. 7 is an example calculated using the minimum-energy phase set for 12 satellites. The main peaks are almost nonexistent here and peculiar thin peaks appear instead, which would seem to be unreasonable. The failure is likely to be due to *both* the non-unique nature of the 1D phase recovery algorithm and the ambiguous determination of relative

phases for the Fourier harmonics. We may not have found a plausible combination of 12 relative phases (or signs) because we may have used the wrong solutions of the individual satellites. Non-uniqueness is an intrinsic property of the 1D Petrashen-Chukhovskii phase recovery algorithm. Attempts at using a reduced data set with 6 lowest-order satellites and examining all 64 possible sign combinations for these reflections resulted in similarly unreasonable maps.

5. Discussion

In the previous study (Nikulin, Sakata, Hashizume *et al.*, 1994), we checked the determined lattice distortions by back calculating triple-crystal rocking curves with the Takagi formula (Takagi, 1969). We use the same technique here. Fig. 8 compares the calculated ω-slice scans for the oxide-removed sample with the observations at $2\theta = \pm 15.84$ arc sec. The agreement is very good except in the central regions. A similarly good agreement was found for $2\theta = 0.0$ arc sec. The higher observed intensities in the central regions may be ascribable to the $\lambda/3$ contamination in the primary X-ray beam. The relative contributions of the $\lambda/3$ harmonic are more important in the near-Bragg regions where a large number of aluminum attenuator foils had to be employed to bring the measured count rates to within the linear range of the NaI scintillation detector. A calculation using Takagi equations, where we put $\chi_{-h} = 0$ to suppress the backward X-ray scattering, was found to fit the envelope of the oscillatory rocking curve in Fig. 8, but with a discrepant central peak height. The Takagi equations with $\chi_{-h} = 0$ provide a kinematic description of diffraction (Davis, 1991), involving no dynamical interference effects in the rocking curve.

We note here, however, that indistinguishable rocking curves result from different strain maps calculated using distinct signs for the 11 satellite reflections. The rocking curve is essentially the Fourier transform of

the Patterson function for the strain distribution and involves a similar "phase problem" to that encountered in conventional crystallography. Many strain distributions can give the same rocking curve just by changing the phase of the reflectance (complex amplitude whose modulus squared gives reflectivity), which is the analogue of structure factor. Each reflection of an imperfect crystal has its own phase problem. The similarity of simulated rocking curves to the observations is thus not a useful measure to select among possible strain models. Some reservation may be needed in accepting strain maps determined by just fitting rocking-curve data (Servidori & Fabbri, 1993; Sluis, Binsma & Dogen, 1993; Klappe & Fewster, 1994).

In the previous paper, we justified the application of a kinematical theory to diffraction from bulk ion-implanted crystals by comparing the thickness of the investigated surface layers with the extinction distance (Nikulin, Sakata, Hashizume *et al.*, 1994). The latter distance is 0.6 μm in the present experiment, which is again approximately equal to the layer thickness studied here. The agreement of the rocking curves calculated using the dynamical and "kinematical" Takagi equations provides evidence that the reconstructed maps are not significantly affected by dynamical effects.

The large strain peaks observed in our maps would represent deposited B^+ ions, which lost their energy in collisions with the silicon lattice and other atoms, as well as clusters of atoms and vacancy complexes. Monte-Carlo calculations by Hobler (1995) show a boron concentration peak at 0.5 μm below the silicon surface, which is slightly deeper than our observation. The majority of the deposited borons would be in substitutional sites: interstitial borons are low in diffusion energy (0.6 eV) and not stable at room temperature (Watkins, 1975). Single silicon interstitials and vacancies are known to have even lower activation energies for diffusion, and thus Si defects can exist only in cluster forms. We note that the X-ray strain profile is much sharper than the Monte-Carlo boron concentration profile in the

depth direction. One can speculate that the different profiles may provide information on the distribution of silicon clusters and vacancy complexes. We have to be careful, however, because our 2D maps are not unique but subject to the ambiguity and artifact problems. Further studies are needed to obtain detailed structure information from reconstructed maps.

A complication with the current 2D reconstruction technique is the interplay between the non-unique solutions from the 1D phase recovery algorithm and the ambiguous relative phases assigned to satellites. This reduces the effectiveness of any figure of merit (FOM) devised for the relative-phase determination. Provided with highly probable solutions of individual satellites, one could apply a maximum-entropy FOM, similar to the ones developed for conventional crystallography (Bricogne, 1993), but based on lattice distortion rather than electron density. Such an FOM is not dependent on the thermal state of the crystal and can be founded on a more sound basis than the minimum-energy FOM. The maximum-entropy method would also be useful in generating maps with spatial resolutions not limited by the data resolution in the lateral direction (Nikulin, Sakata, Hashizume *et al.*, 1994).

We now argue why we failed in procuring acceptable maps for the oxide-covered sample while we succeeded in the oxide-removed sample using the same technique. Our ion-implanted sample with the mask oxide pattern existing on the surface involves very complicated lattice distortions with large strain gradients, as evidenced by the enhanced satellite intensities. The strain fields due to the deposited ions and the oxide film edges add up in thin near-surface layers. In such a crystal the Bragg intensity of each Fourier harmonic would be locally minimal at a large number of q values, where the Bragg wave undergoes phase shifts in the Petrashen-Chukhovskii phase recovery algorithm. These minima yield complex zeros in the mathematical treatment of the intensity data (Nikulin, Sakata, Hashizume *et al.*, 1994). It is difficult to distinguish such zeros from those introduced by a

polynomial function used to fit the intensity data and to choose plausible solutions among the multisolutions of the Petrashen-Chukhovskii algorithm.

The technique used in this study for mapping two-dimensional lattice strain only applies to distortions having lateral periodic superstructure modulations. Clearly, this limitation is associated with the two-step procedure which first retrieves the phase information for individual harmonic waves and then synthesizes the solutions. A truly two-dimensional phase retrieval would lift this limitation and be applicable to general distortions. It should also reduce the need for prior knowledge about the sought structure, as well as the degree of subjectivity, conscious and unconscious, and arbitrariness, in the decision process. Attempts are under way in this direction.

We are grateful to G. Hobler for the calculation of the boron concentration profiles. Assistance from G. Foran and R. Garrett in the experiment is acknowledged. Discussion with M. Suezawa was valuable for the interpretation of the obtained maps. X-ray experiments described in this paper were supported by the Photon Factory under proposal 92G261. We also appreciate the support of the ANBF. The ANBF is funded by a consortium comprising ARC, DIST, ANSTO, CSIRO, UNSW and ANU. AYN and TEG acknowledge the support from the ARC. This work was supported by a Monbusho International Scientific Research Program (contract No. 04044066).

References

Barnea, Z., Clapp, R., Creagh, D.C., Sabine, T.M., Stevenson, A.W., White, J.W., Wilkins, S.W., Harada, J., Hashizume, H., Kashihara, Y., Sakata, M., Ohsumi K. & Zemb T. (1989). *Rev. Sci. Instrum.* 60, 2537-2540.

Barnea, Z., Creagh, D.C., Davis, T.J., Garrett, R.F., Janky, S., Stevenson A.W. & Wilkins S.W. (1992). *Rev. Sci. Instrum.* 63, 1069-1072.

Bricogne, G. (1993). *Acta Cryst.* D 49, 37-60.

Davis, T.J. (1991). *Aust. J. Phys.* 44, 693-704.

Goureev, T.E., Nikulin, A.Yu. & Petrashen, P.V. (1992). *Phys. Status Solidi* A 130, 263- 271.

Hobler, G. (1995). Unpublished.

Klappe, J.G.E. & Fewster, P.F. (1994). *J. Appl. Cryst.*, 27, 103-110.

Millane, R.P. (1990). *J. Opt. Soc. Am.* A7, 394-411.

Nikulin, A.Yu., Sakata, O., Hashizume H. & Petrashen, P.V. (1994). *J. Appl. Cryst.* 27, 338-344.

Nikulin, A.Yu., Stevenson, A.W., Hashizume, H., Wilkins, S.W., Cookson, D., Foran, G. & Garrett, R.F. (1995). *J. Appl. Cryst.*, 28, 57-60.

Nye J.F., Physical Properties of Crystals (Clarendon Press, Oxford, 1985).

Petrashen, P.V & Chukhovskii F.N. (1989). *Sov. Phys. Dokl.* 34, 957-959.

Servidori, M. & Fabbri, R. (1993). *J. Phys. D, Appl. Phys.*, 26, A22-A28.

Sluis, P., Binsma, J.J.M. & Dogen, T. (1993). *Appl. Phys. Lett.*, 62, 3186-3188.

Takagi, S. (1969). *J. Phys. Soc. Japan*, 26, 1239-1253.

Watkins, G.D. (1975). *Phys. Rev.* B12, 5824-5839.

Figure captions

Fig. 1. Experimental set-up for triple-crystal diffractometry using "BIGDIFF" at beamline 20B of the Photon Factory synchrotron source. The large drum housing the diffractometer can be evacuated to reduce air scatter.

Fig. 2. Gray-scale representation, on a logarithmic scale, of intensity distributions in reciprocal space for the Si (111) sample without SiO_2 layer. The Bragg peak is located at $q_x = q_z = 0$. The jagged appearance of the crystal-truncation-rod streaks, nearly parallel to the q_z axis, is an artifact, as well as isolated black spots.

Fig. 3. ω-slice scans through the Bragg peaks for the case where the surface oxide layer is (a) present and (b) removed. The data have been scaled so that the maxima for the data sets correspond to the calculated peak reflectivity values for a perfect Si(111) crystal.

Fig. 4. CTR intensity distributions associated with the fundamental ($n = 0$) and satellite ($n = 1$ to 11) reflections, observed from the ion-implanted Si sample (a) with and (b) without SiO_2 layer. The satellite curves are vertically shifted to avoid overlaps.

Fig. 5. 2D strain maps reconstructed for the Si (111) crystal implanted with 100 keV boron ions through a periodic surface oxide mask pattern which was removed before X-ray data collection. The relative phases of 11 satellite reflections were determined with (a) the sequential trial method and (b) minimum-energy method. Thick black lines on the surface axis indicate the location and size of the removed oxide strips.

Fig. 6. Gray-scale representation of the strain map in Fig. 5(a). Satellite signs were determined with the sequential trial method.

Fig. 7. Failed 2D strain map for the ion-implanted Si (111) sample with the oxide layer present on the surface.

Fig. 8. Calculated (line) and observed (data points) ω-scan rocking curves for the oxide-removed sample for analyzer position (a) $2\theta = -15.84$ and (b) +15.84 arc sec.

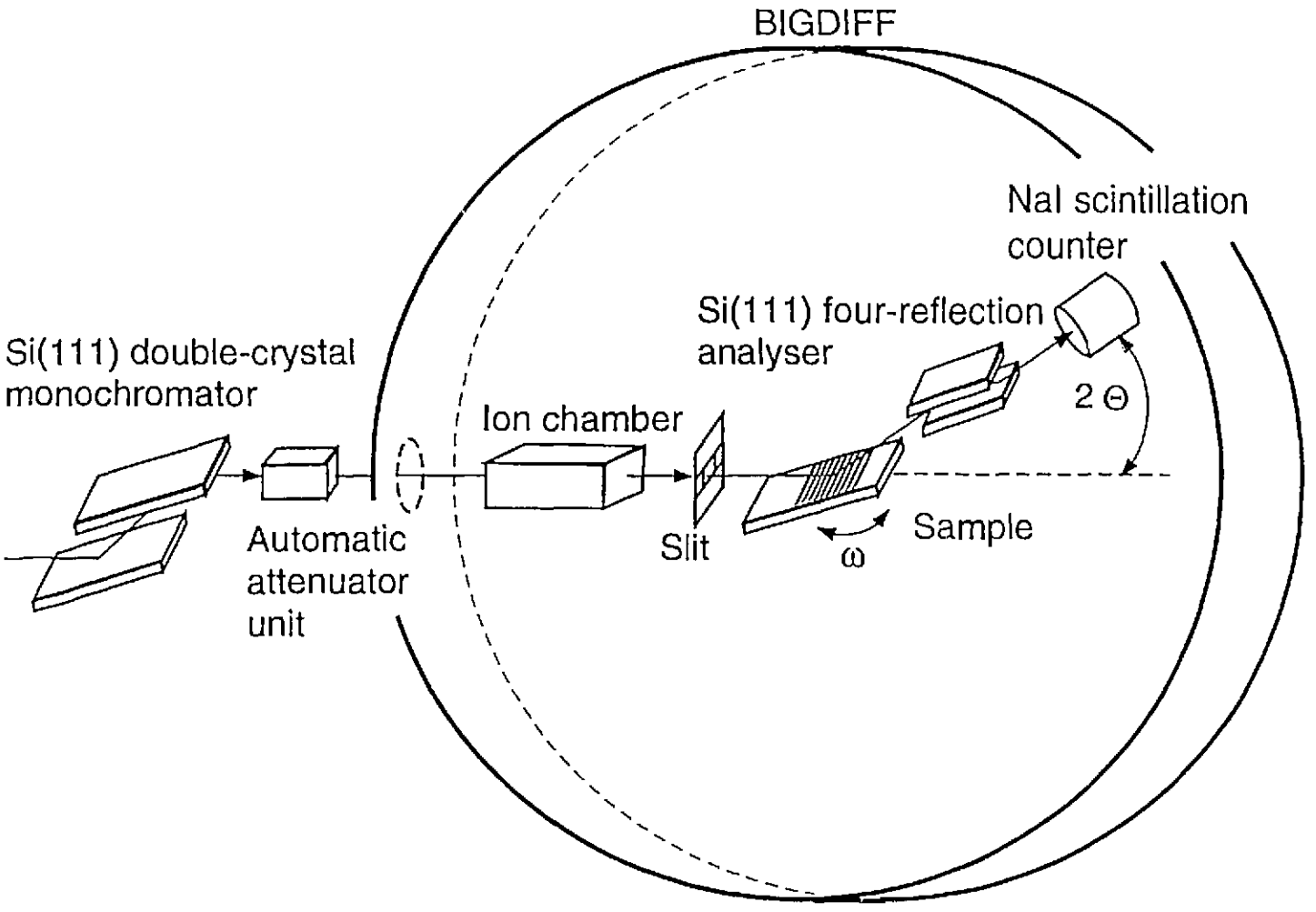

Fig. 1. Nikulin et al.

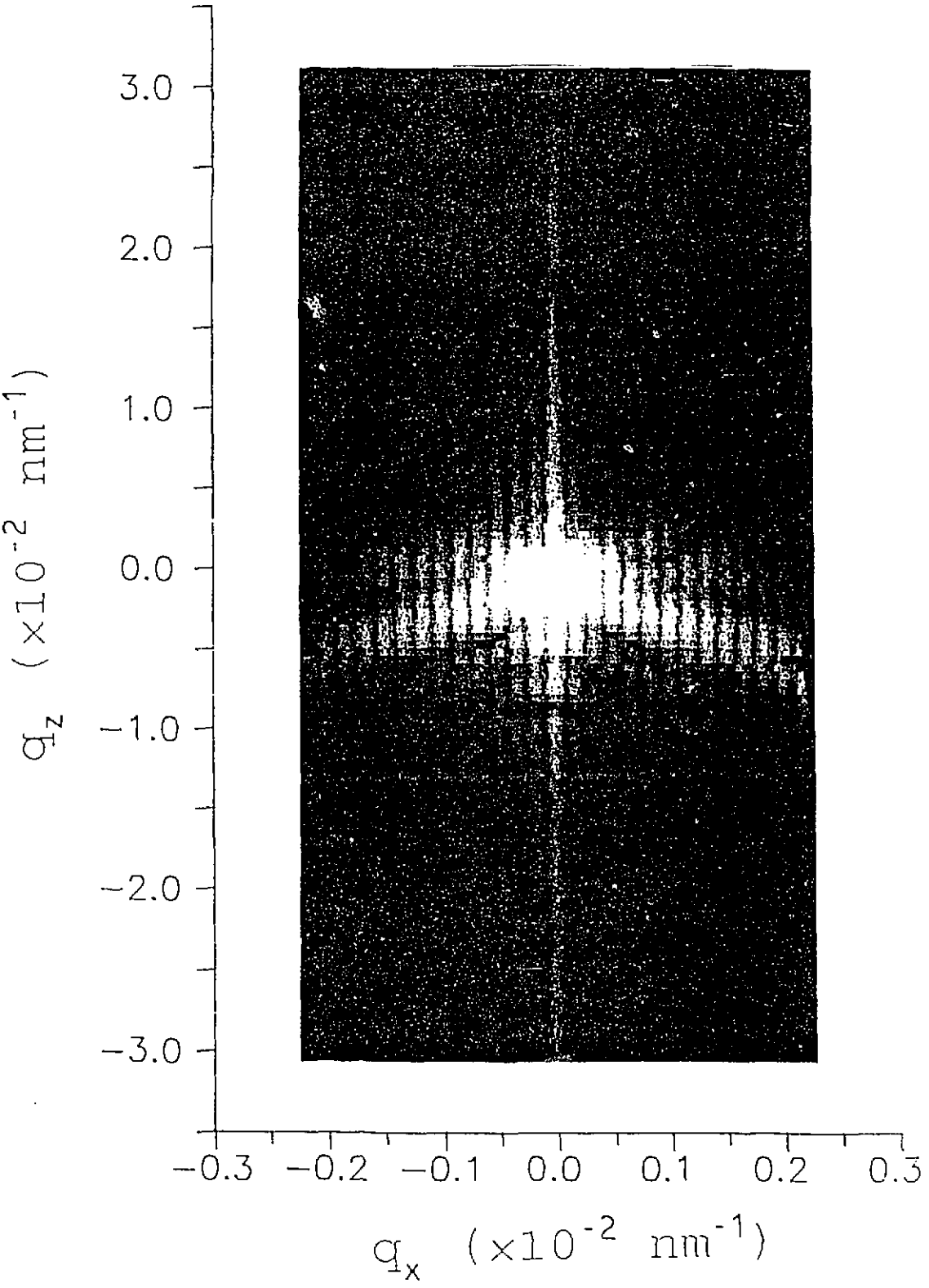

Fig. 2 Nikulin et al.

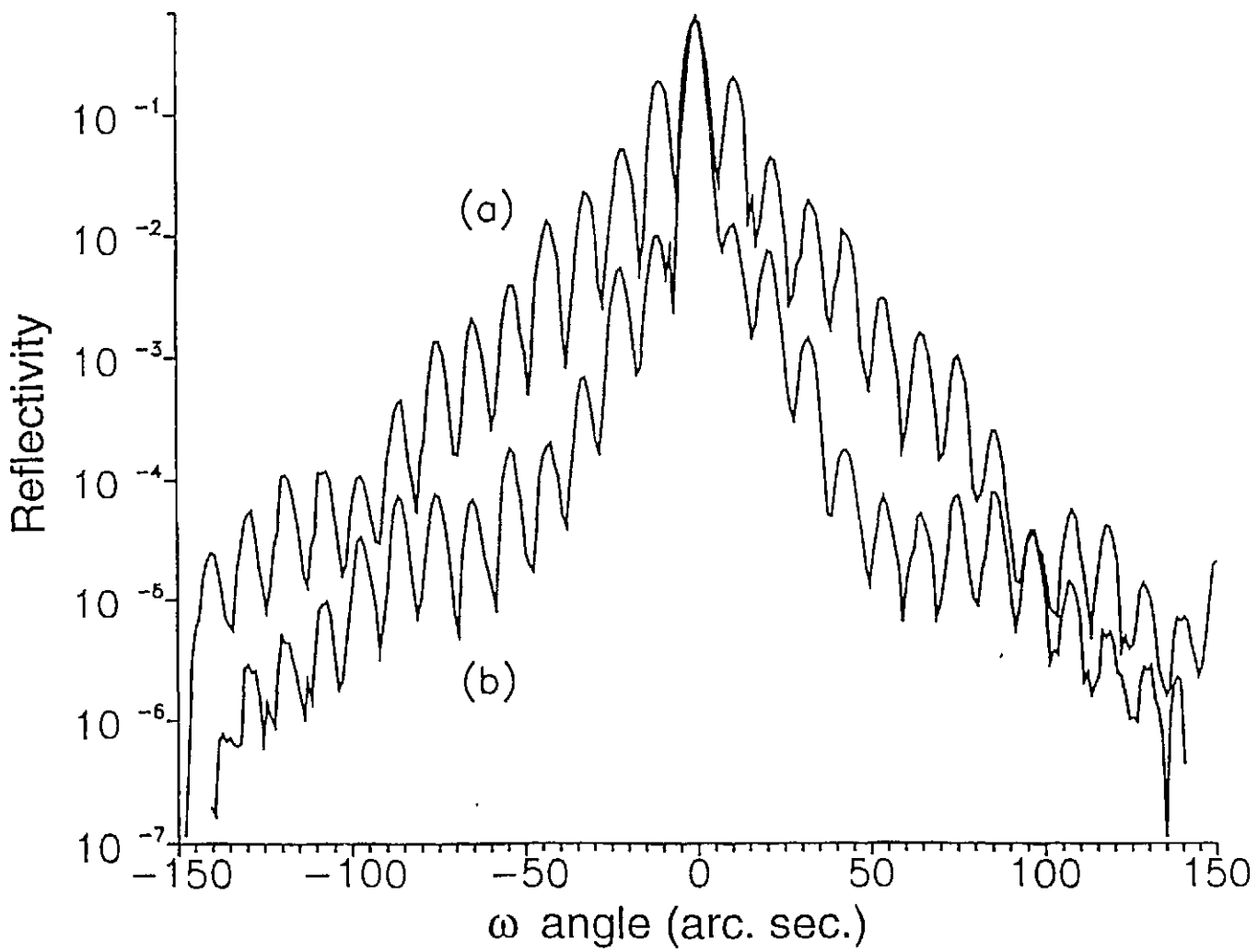

Fig. 3 Nikulin et al.

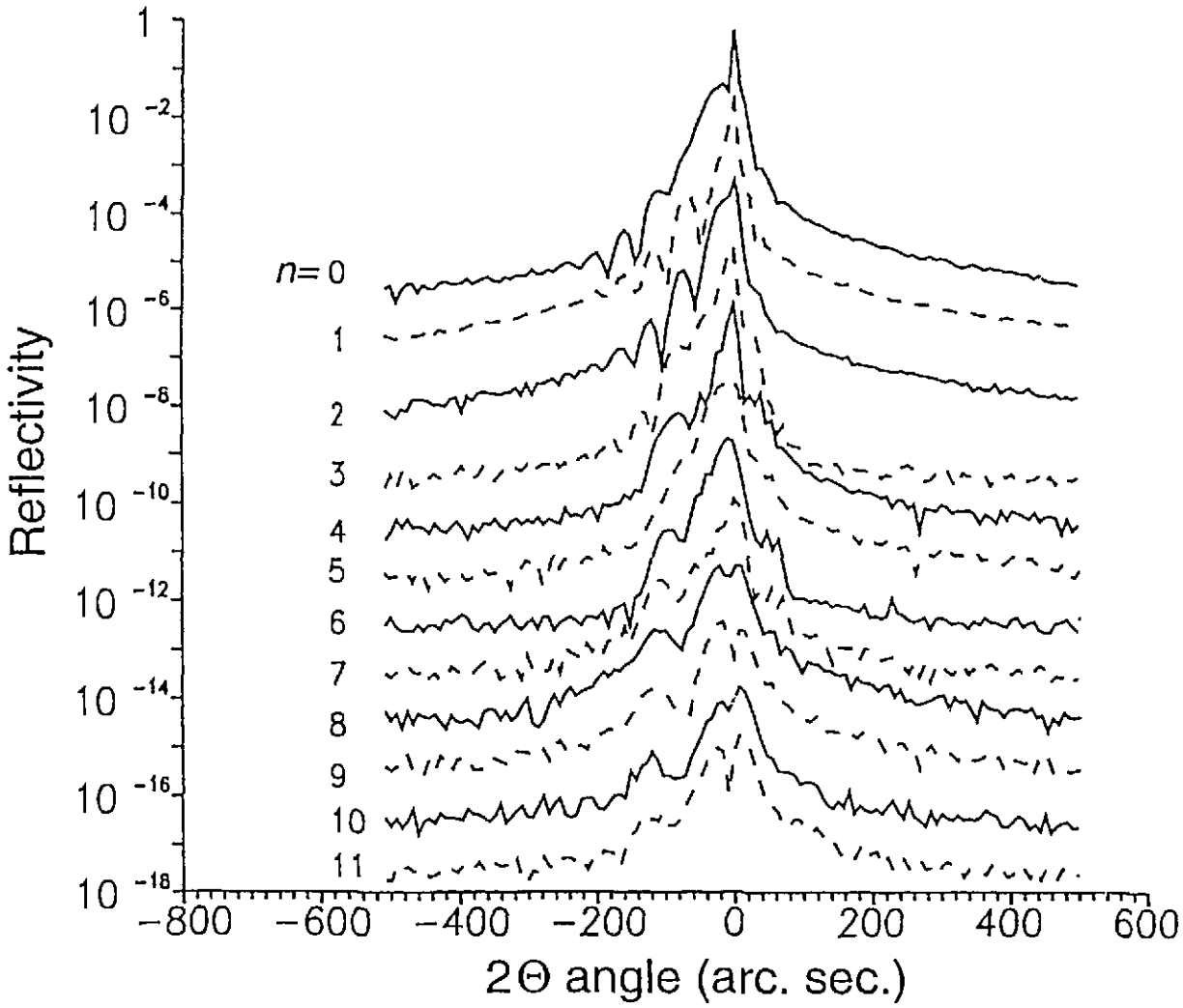

Fig. 4a Nikulin et al.

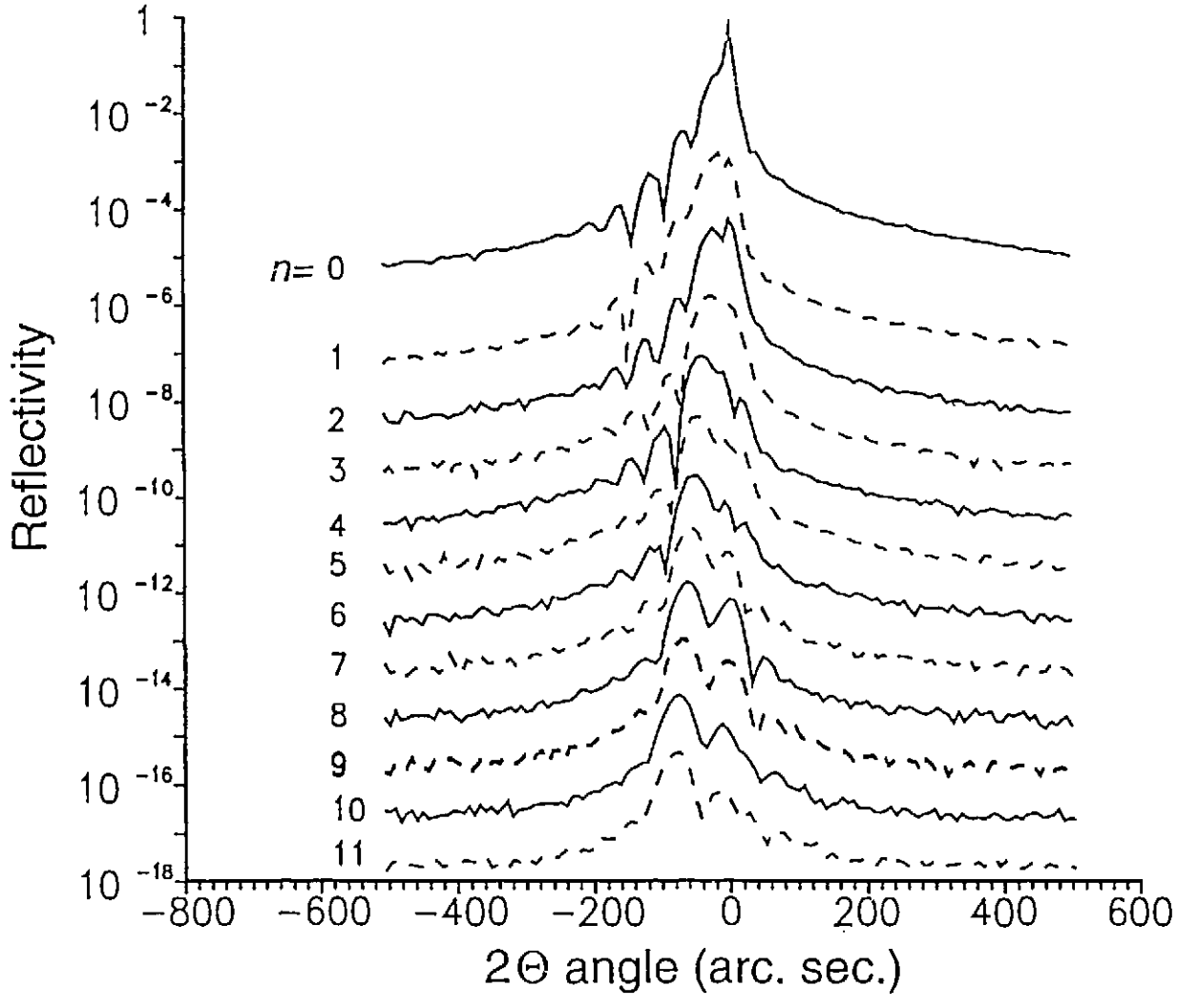

Fig. 4b Nikulin et al.

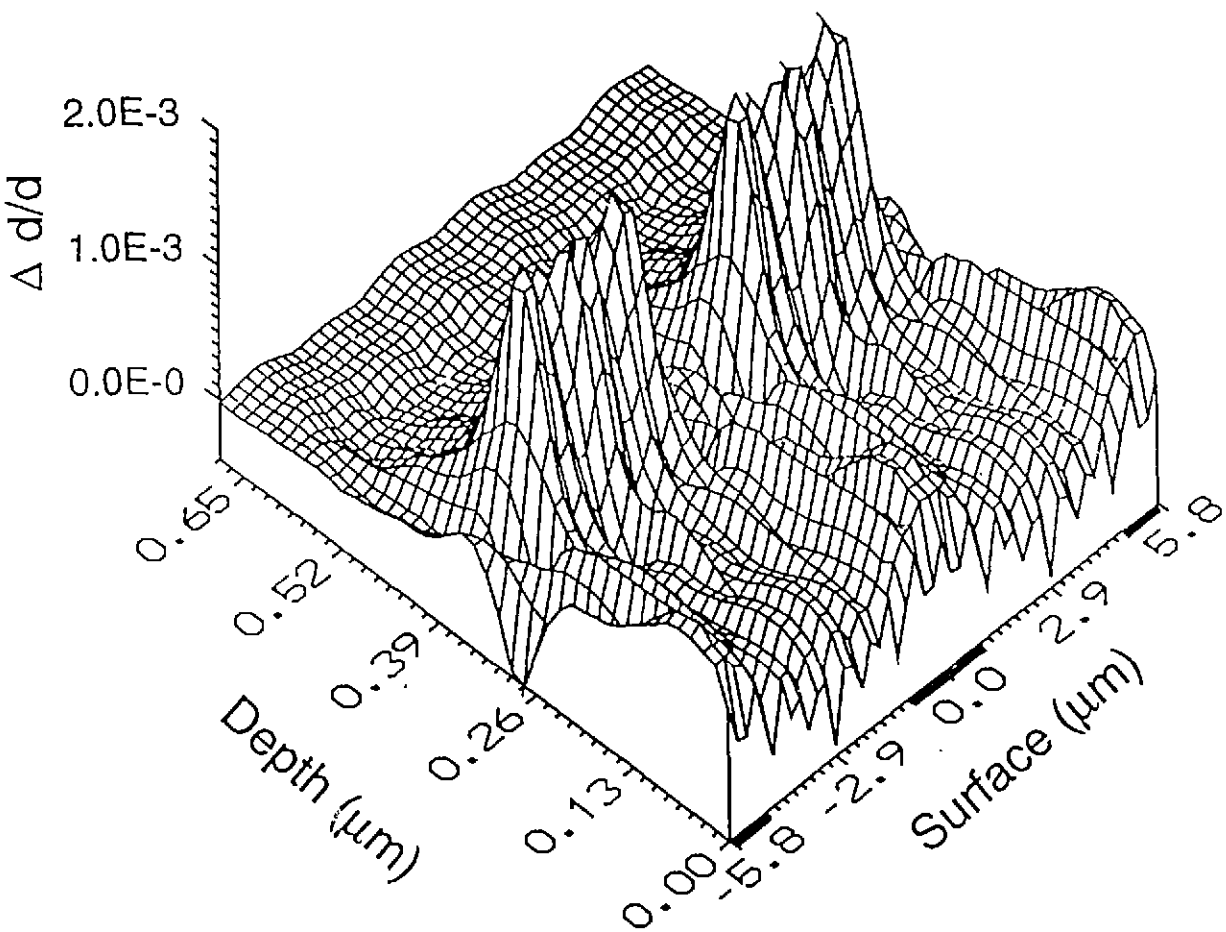

Fig. 5a Nikulin et al.

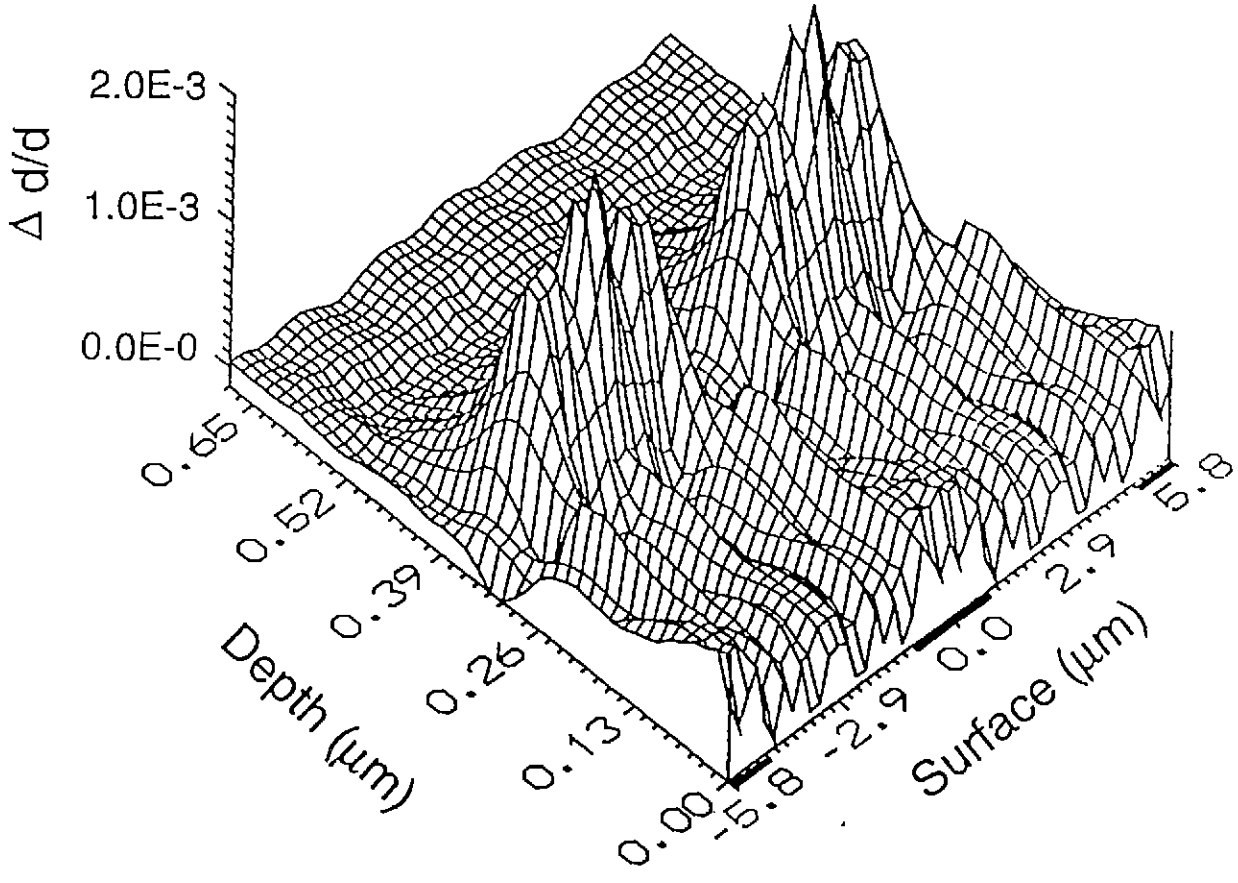

Fig. 5b Nikulin et al.

Fig. 6 Nikawa et al.

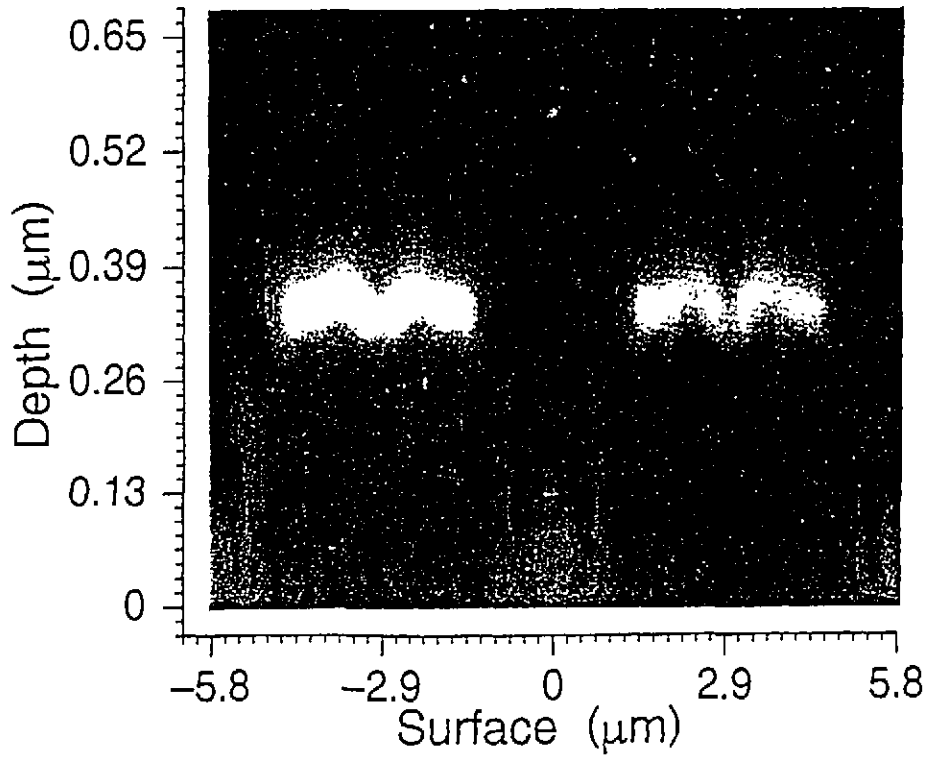

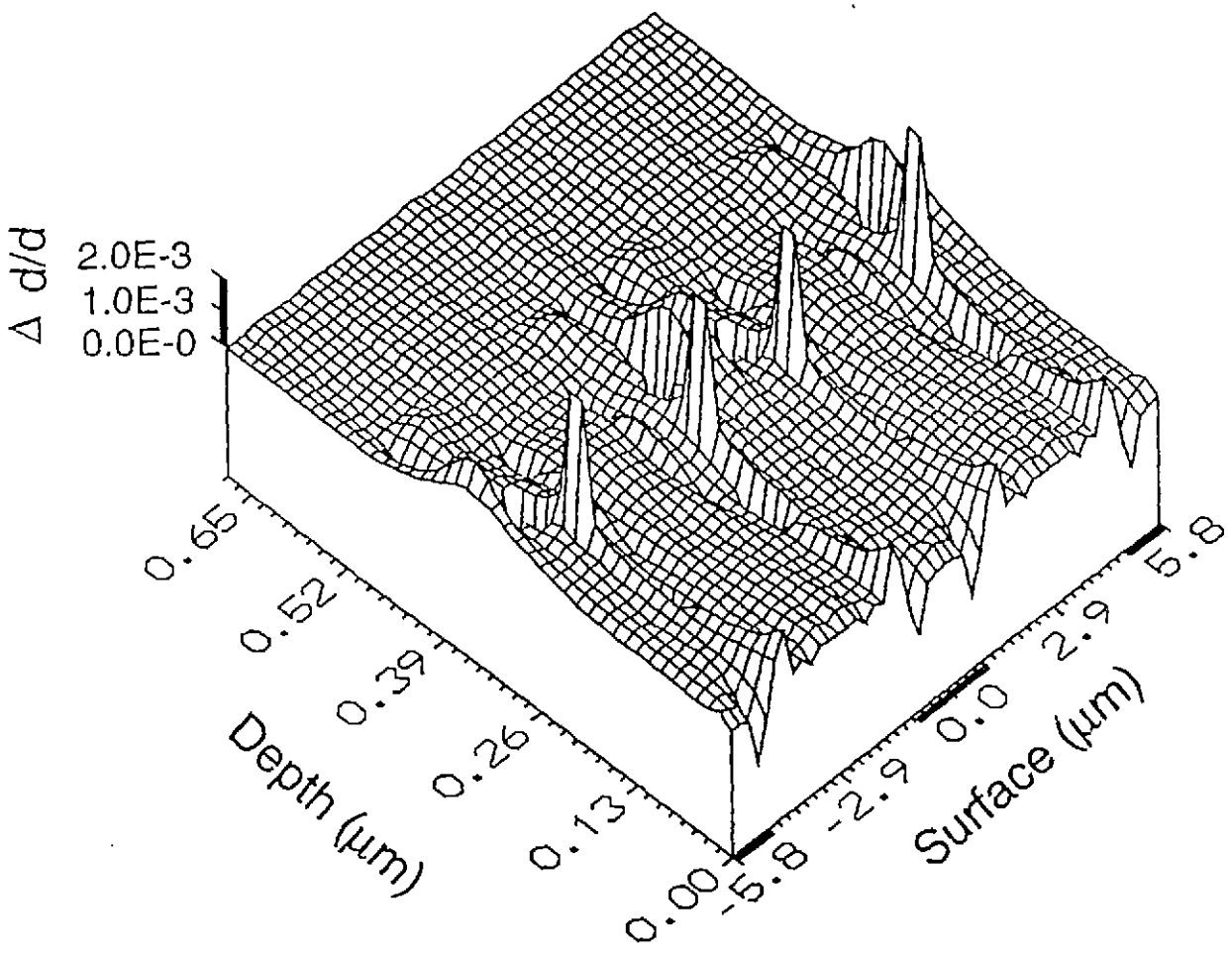

Fig. 7 Nikulin et al.

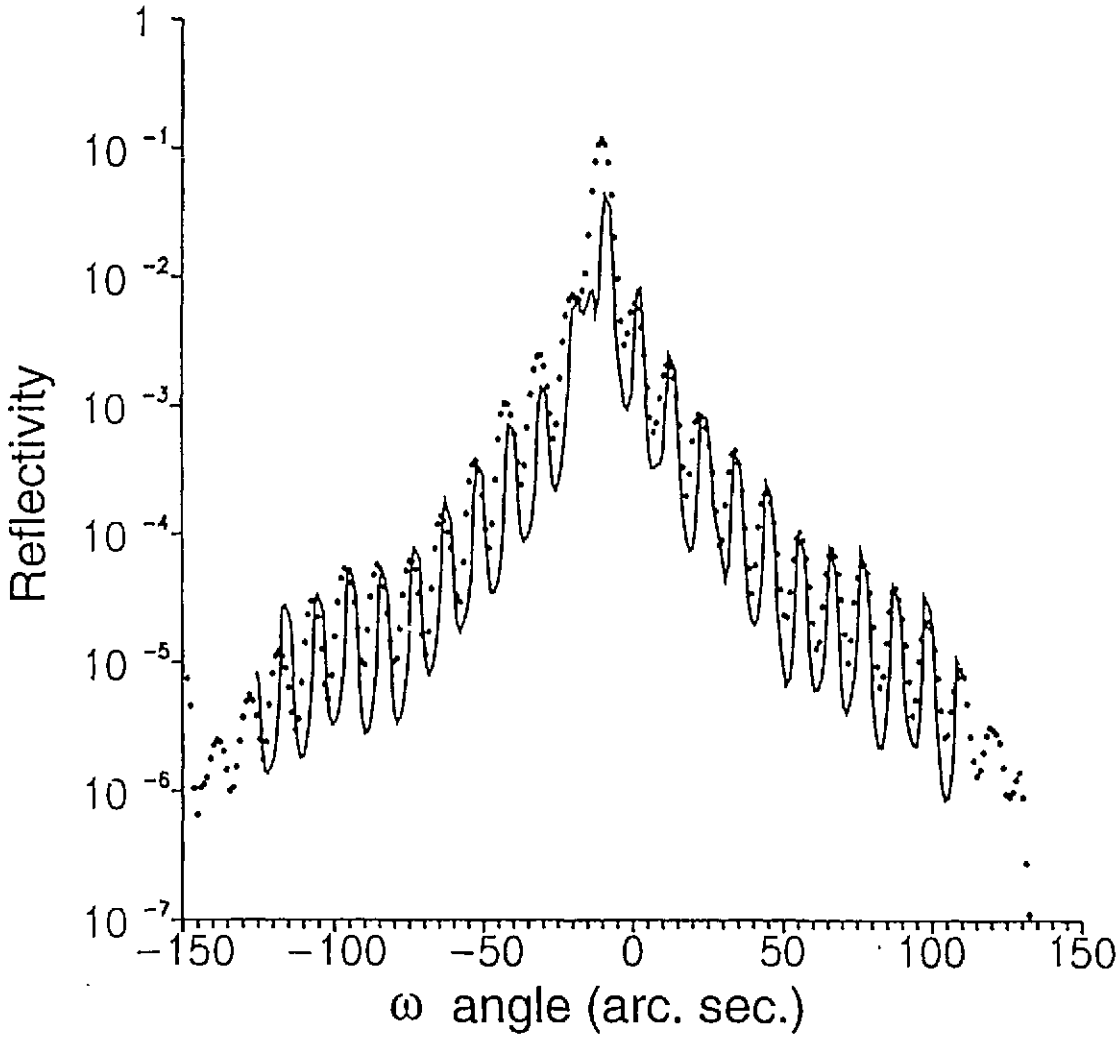

Fig. 8a Nikulin et al.

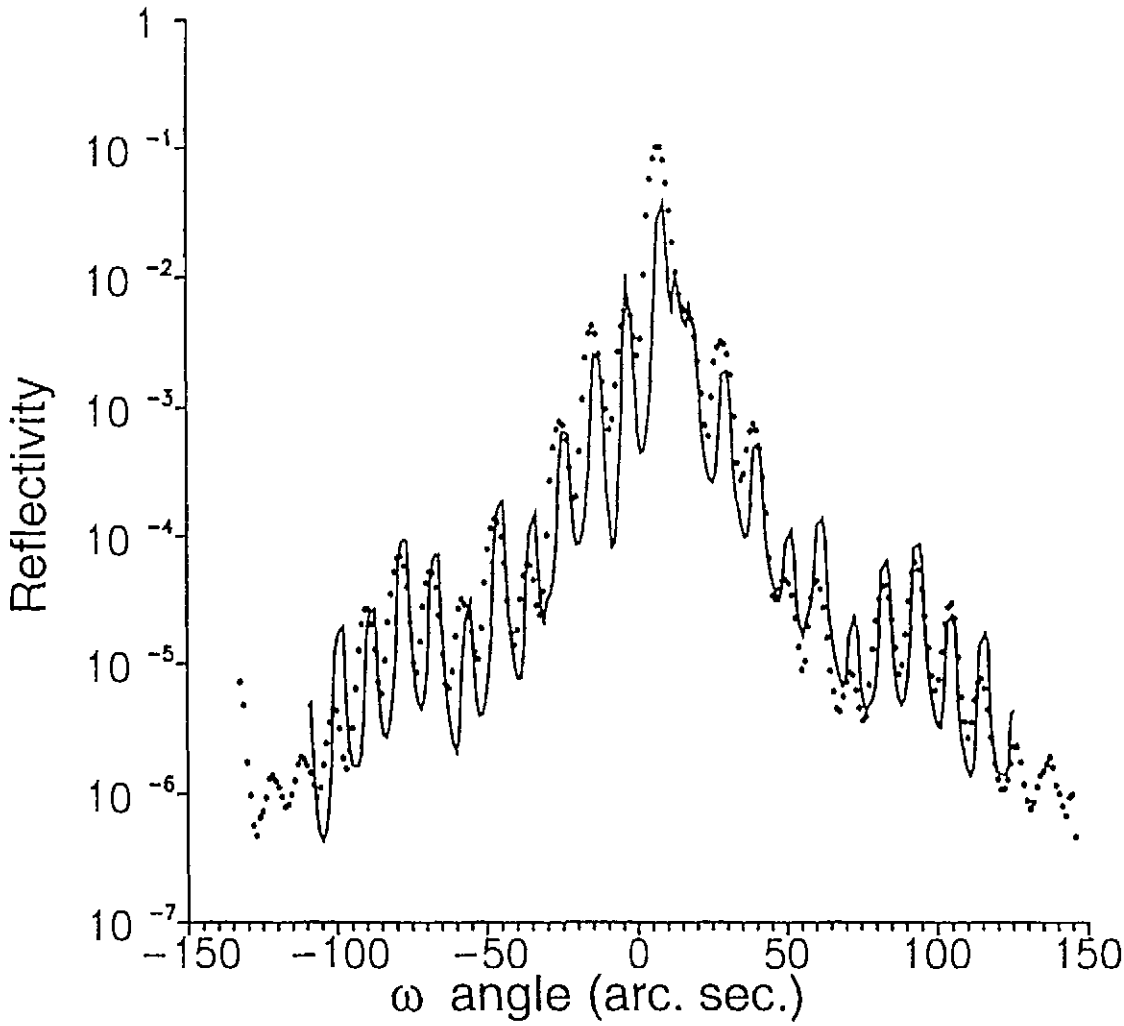

Fig. 8b Nikulin et al.